Journal of Applied Physics ARTICLE scitation.org/journal/jap

A generic theoretical approach for estimating bandgap bounds of metamaterial beams

Cite as: J. Appl. Phys. **130**, 054501 (2021); doi: 10.1063/5.0053004
Submitted: 3 April 2021 · Accepted: 22 July 2021 ·
Published Online: 5 August 2021

Yupei Jian,[1] Guobiao Hu,[1,2] Lihua Tang,[1,a)] Jiawen Xu,[3] and Kean C. Aw[1]

AFFILIATIONS

[1]Department of Mechanical Engineering, The University of Auckland, Auckland 1010, New Zealand
[2]School of Civil and Environmental Engineering, Nanyang Technological University, Singapore 639798, Singapore
[3]School of Instrument Science and Engineering, Southeast University, Nanjing 210096, China

[a)]**Author to whom correspondence should be addressed:** l.tang@auckland.ac.nz

ABSTRACT

The bandgap phenomenon in metamaterials has attracted much research interest for controlling structural vibrations. To tailor the bandgap for applications in a specific frequency range, analytical tools for bandgap bound estimations are critically important. This work presents a generic theoretical approach for fast estimation of the bandgap bounds. Starting from the lattice metamaterial systems, we develop the procedure and provide the analytical bound expressions based on a hypothesis of extreme points in the band structure of metamaterial systems. The proposed approach for the lattice system is verified by the results of transmittance analysis. Subsequently, to explore the fidelity of the proposed approach on continuous metamaterial systems, three typical metamaterial beams (metabeams) have been investigated: a metabeam with mechanical local resonators, a piezoelectric metabeam with shunt resonant circuits, and a hybrid metabeam. Finite element analysis is performed to verify the theoretical expressions of bandgap bounds derived using the proposed approach. With the verified bound expressions, bandgap tailoring and optimization are further investigated. In summary, the developed theoretical approach is generic and offers a promising technique for bandgap estimation of metamaterial systems integrated with various types of resonators.

I. INTRODUCTION

In recent decades, locally resonant metamaterials have been widely researched. The introduction of local resonators alters the physical property of materials, which gives rise to some features that could not be found in natural materials, including effective negative mass density[1] and effective negative modulus.[2] Meanwhile, similar to Bragg scattering phononic crystals,[3] the bandgap phenomenon also exists in locally resonant metamaterials, or "metamaterials" for short. Unlike Bragg scattering induced bandgaps in phononic crystals, which strongly depend on the lattice periodicity, local resonance induced bandgaps in metamaterials are almost insensitive to periodicity and resilient to randomness. The frequency range of a local resonance induced bandgap is roughly determined by the natural frequency of the local resonator. This feature means that the locally resonant bandgap can be theoretically produced at arbitrarily long wavelengths, making metamaterials suitable candidates for low-frequency vibration attenuation at relatively small sizes.[4–6] To date, researchers have devoted increasing efforts to integrating metamaterial design into practical mechanical structures for low-frequency vibration attenuation. For example, locally resonant metamaterial beams (metabeams) with periodically attached resonators have been studied extensively.[7–9] The width of a local resonance induced bandgap depends on the resonator mass, implying that a broader bandgap width would require a larger resonator mass. To avoid significant weight increase, researchers have considered introducing multiple local resonances to generate multiple bandgaps to widen the vibration attenuation range. The multiple local resonances could be achieved by multiple degree-of-freedom (DOF) resonators[10,11] or arrays of resonators with different resonant frequencies.[7,12,13] For example, Zhu *et al.*[7] proposed a chiral elastic metamaterial beam by embedding multiple local resonators. Broadband vibration attenuation can be achieved by using section-distributed unit resonators. In addition, the nonlinear bandgap behavior of nonlinear metamaterials has also attracted attention. Using spectro-spatial analysis, Zhou *et al.*[14] investigated the solitary wave in the short-wavelength region of a nonlinear metamaterial. On the other hand, to reduce the additional mass brought by mechanical resonators, piezoelectric metamaterial systems are proposed. Due to

the electromechanical coupling effect of piezoelectric materials, an electrical circuit-induced resonance could induce a reaction force/moment on the mechanical structure. Hence, a shunt circuit resonance is analogous to a mechanical resonator. Many studies focused on exploring different types of shunt resonant circuits to realize broadband vibration attenuation, such as the pure inductance circuit,[15] negative capacitance circuit,[16,17] high-order resonant circuit,[18] and digital feedback circuit,[19–21] to name a few. More recently, by combining the mechanical and the electrical resonance mechanisms, hybrid metamaterials were demonstrated to exhibit negative effective mass density and negative bending stiffness properties simultaneously.[22,23]

From the practical application point of view, it is necessary to gain insights into the influences of material properties on bandgap formation in metamaterials. In other words, developing bandgap estimation approaches is important for the design and optimization of metamaterials. A mass-in-mass lattice model is widely adopted to represent the acoustic metamaterial, and the frequency region for the effective mass being negative is used to approximately indicate the bandgap.[16,24] For the distributed parameter model, many researchers investigated the band structure behavior using the transfer matrix method.[5,25] The dispersion relation of waves propagating in the metamaterials can be predicted using the transfer matrix method, and the bandgaps can then be identified from the dispersion curve patterns. The extended Hamilton principle was another alternative approach utilized to derive the dispersion relation of wave propagation in metabeams.[26,27] However, most previous works identified bandgap locations by observing the blank areas in the dispersion curve patterns. How to directly compute the bandgap bounds is still a fundamental but challenging problem. Based on the wave equation, Xiao *et al.*[28] investigated the flexural wave propagation in an infinite metamaterial with mechanical resonators using the spectral element method. By expanding the spectral matrix, they derived specific bandgap bound equations associated with a certain material parameter by fixing the others. More recently, the derivation of bandgap bound equations in Ref. 28 was further improved and gave a more general closed-form expression by using Taylor's expansion to eliminate the trigonometric functions.[29] From the viewpoint of modal analysis, Sugino *et al.* developed a novel approach to estimate the bandgap formation in finite-length metabeams attached with mechanical resonators,[30] electromechanical resonators,[31,32] and hybrid resonators.[22] The assumption of an infinite number of resonators was used in conjunction with the orthogonality condition to simplify the modal equations. The closed-form bandgap bound equations were successfully derived. This approach could also provide insights into how the resonators affect the mode shapes of a finite-length metabeam.

In this paper, we present a new generic theoretical framework for fast bandgap estimation. By analyzing the topology of the dispersion relation for different metamaterial models, the slope of the angular frequency at the bandgap bound is observed to be zero. Consequently, we are inspired to locate the bandgap bounds and derive their analytical expressions by seeking "extreme points" of the dispersion curves. A rigorous mathematical proof has been provided for this hypothesis. To the best of the authors' knowledge, this is the first attempt to locate the bandgap bounds in this way. The merits of this approach lie in that the derivation process is simple and straightforward. Mathematical simplification through the orthogonality condition or Taylor's expansion is not needed. Moreover, several case studies, from discrete lattice models to beam-type continuous models, have demonstrated that this approach is generic and applicable to various metamaterial systems. It is worth mentioning that some models in the case studies are well known to the metamaterial research community and have also been used in Refs. 22 and 29–32. The novelty of this work lies in the generic theoretical framework for bandgap analysis, while these well-known models are just adopted for demonstration.

The remainder of this article is divided into five sections. In Sec. II, the universal definition of the bandgap bound is described based on the dispersion relation analysis of the infinitely long lattice model and the extreme theory. A systematic solution procedure is developed to derive the bandgap bound equations. Subsequently, to reveal the robustness of the proposed approach, the procedure is applied to three typical types of metabeams, namely, a metabeam with mechanical local resonators, a piezoelectric metabeam with shunt resonant circuits, and a hybrid metabeam combining mechanical and circuitry resonance mechanisms. The bound equations corresponding to the considered models are derived. In Sec. III, the corresponding finite element (FE) models of the three metabeams are established, followed by the validation of the derived equations in Sec. IV. The results from Ref. 31 are also taken into comparison. Section V further discusses the merits of the proposed approach in terms of tailoring and optimization of bandgaps. An extended case is presented to further demonstrate the universality of the proposed approach for handling more complicated metamaterial systems. Finally, conclusive remarks are drawn in Sec. VI.

II. THEORETICAL FORMULATION

A. Estimation of bandgap bounds of a conventional infinite lattice system

A conventional metamaterial model, i.e., an infinite mass-in-mass lattice system (Fig. 1), is first adopted to introduce the approach for fast estimating bandgap bounds. Such a discrete model is widely adopted in the literature to represent locally resonant metamaterials (see, for example, Ref. 33). Each unit cell consists of an outer spherical shell m_1 and an inner mass m_2, connected by an inner spring k_2. The adjacent spherical shells are uniformly placed at a distance d and connected by a spring k_1 to form a lattice chain. For harmonic wave propagation in this system, the equations of motion for the jth unit cell are

$$\begin{cases} m_1\ddot{u}_1^{(j)} + k_1(2u_1^{(j)} - u_1^{(j-1)} - u_1^{(j+1)}) + k_2(u_1^{(j)} - u_2^{(j)}) = 0, \\ m_2\ddot{u}_2^{(j)} + k_2(u_2^{(j)} - u_1^{(j)}) = 0, \end{cases} \tag{1}$$

where the harmonic wave solutions $u_1^{(j)} = A_1 e^{i(qx-\omega t)}$ and $u_2^{(j)} = A_2 e^{i(qx-\omega t)}$ represent the displacements of masses m_1 and m_2 in the jth cell, respectively. A_1 and A_2 are the wave amplitudes. i is the imaginary unit. q and ω correspond to the wavenumber and angular frequency, respectively. For this periodic structure, the displacements of the masses in the $(j+m)$th cell satisfy the following

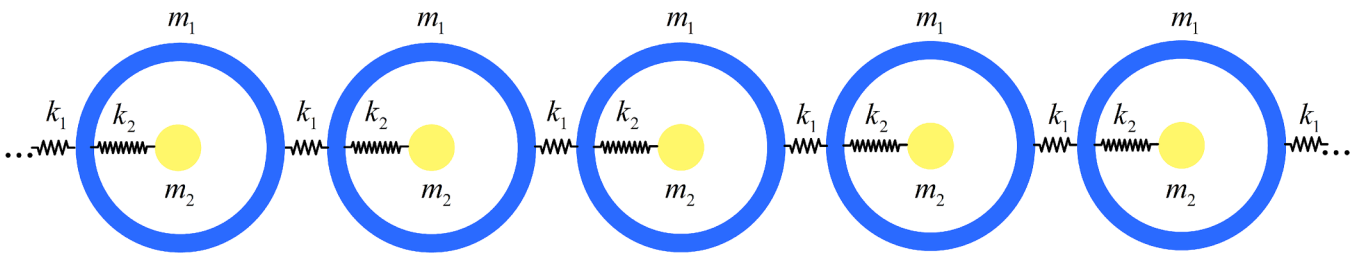

FIG. 1. Conventional infinite lattice metamaterial system.

form according to Bloch's theorem:

$$u_1^{(j+m)} = A_1 e^{i(qx+mqd-\omega t)}, \quad u_2^{(j+m)} = A_2 e^{i(qx+mqd-\omega t)}, \tag{2}$$

where d is the lattice constant. Substituting Eq. (2) into (1), one can obtain the dispersion equation as

$$\begin{aligned} &m_1 m_2 \omega^4 - [k_2(m_1+m_2) + 2k_1 m_2(1-\cos(qd))]\omega^2 \\ &+ 2k_1 k_2(1-\cos(qd)) = 0. \end{aligned} \tag{3}$$

In the band structure analysis, q calculated from Eq. (3) can be classified into three categories: the purely real, purely imaginary, and complex ones, corresponding to the propagation, attenuation, and semi-attenuation frequency regions. The so-called bandgap refers to the frequency range in which no real q exists for a given ω. Since a negative real solution q refers to a wave traveling in the negative direction, only the dispersion curves in the first quadrant of the ω–q plane are of our concern and denoted as r curves. To obtain these curves, Eq. (3) is solved directly. Since Eq. (3) is a quartic equation of ω, two groups of real roots can be obtained directly as

$$\omega_n(qd) = \sqrt{\frac{2k_1m_2 + k_2m_1 + k_2m_2 + (-1)^n\sqrt{A} - 2k_1m_2\cos(qd)}{2m_1m_2}}, \; n = 1,2, \tag{4}$$

where

$$\begin{aligned} A = {} & 4k_1m_2^2(k_1+k_2) + k_2^2(m_1+m_2)^2 + 4k_1^2m_2^2\cos(qd)(\cos(qd)-2) \\ & + 4k_1k_2m_1m_2(\cos(qd)-1) - 4k_1k_2m_2^2\cos(qd) \end{aligned}$$

and $n = 1,2$ denote the r_u and r_l curves, i.e., the upper and lower dispersion curves. To observe the bandgap intuitively, an example with parameters $m_1 = 0.05$ kg, $m_2 = 0.025$ kg, $k_1 = 50$ N/m, and $k_2 = 60$ N/m is demonstrated in Fig. 2.

Due to the periodicity of the structure, the local resonance induced dispersion curve follows a specific pattern: the left and right ends of the first Brillouin zone correspond to the minimum and maximum values of r_l and r_u. For the whole ω–q plane, the dispersion relation periodically repeats its pattern in the first Brillouin zone. The slope of r curve, namely, $d\omega/dq$, represents the group velocity. It can be seen that the group velocity of the curve is equal to zero at the peak E1 of r_l and valley E2 of r_u. Note that the bandgap is located inside the two dispersion curves. The problem of bandgap boundary prediction can be converted into seeking the extreme values of r_l and r_u with derivatives equal to zero. Letting the derivative $\omega_n'(qd) = 0$, two roots can be solved through MATLAB's solve() function:

$$qd_1 = 0, \quad qd_2 = \pi. \tag{5}$$

Substituting qd_1 and qd_2 into $\omega_2(qd)$ and $\omega_1(qd)$, respectively, one can obtain the upper and lower bounds of the bandgap analytically,

$$\begin{cases} b^- = \omega_\beta\sqrt{2\alpha^2 + \frac{1}{2}\mu + \frac{1}{2} - \sqrt{\frac{1}{4}\mu^2\left(\left(4\frac{1}{\mu}\alpha^2 + \frac{1}{\mu} + 1\right)^2 - \left(4\frac{1}{\mu}\alpha\right)^2\right)}}, \\ b^+ = \omega_\beta\sqrt{\mu+1}, \end{cases} \tag{6}$$

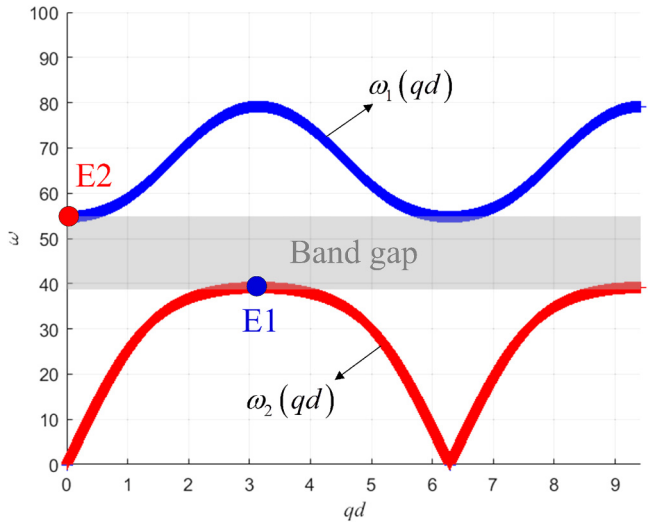

FIG. 2. Band structure of conventional infinite lattice metamaterial system.

where $\mu = \frac{m_2}{m_1}$, $\omega_\alpha = \sqrt{\frac{k_1}{m_1}}$, $\omega_\beta = \sqrt{\frac{k_2}{m_2}}$, $\alpha = \frac{\omega_\alpha}{\omega_\beta}$, and the superscripts $-$ and $+$ denote the lower and upper bounds of the bandgap, respectively. It is worth mentioning that Eq. (6) is different from the widely adopted bandgap bound equation in Refs. 16 and 33,

$$\begin{cases} b^- = \omega_\beta, \\ b^+ = \omega_\beta\sqrt{\mu+1}. \end{cases} \tag{7}$$

In these references, the bandgap is believed to be consistent with the frequency range in which the effective mass $m_{eff} = m_1 + m_2/(1-(\omega/\omega_\beta)^2)$ of this lattice system becomes negative. For example, Fig. 3 depicts the dimensionless effective mass with the varying dimensionless angular frequencyω/ω_β. The effective mass turns out to be negative when $\omega > \omega_\beta$ and becomes positive again when $\omega > \omega_\beta\sqrt{\mu+1}$, leading to Eq. (7).

The accuracies of Eqs. (6) and (7) are verified by comparing them with the transmittance results of the finite lattice system. Figure 4 shows the schematic of the conventional finite lattice metamaterial system with n cells. Except for the first and last unit cells, the equations of motion of the jth unit cell are

$$\begin{cases} m_1\ddot{u}_1^{(j)} + k_1(2u_1^{(j)} - u_1^{(j-1)} - u_1^{(j+1)}) + c_1(2\dot{u}_1^{(2j+1)} - \dot{u}_1^{(j-1)} - \dot{u}_1^{(j+1)}) + k_2(u_1^{(j)} - u_2^{(j)}) + c_2(\dot{u}_1^{(j)} - \dot{u}_2^{(j)}) = 0, \\ m_2\ddot{u}_2^{(j)} + k_2(u_2^{(j)} - u_1^{(j)}) + c_2(\dot{u}_2^{(j)} - \dot{u}_1^{(j)}) = 0, \end{cases} \tag{8}$$

where c_1 and c_2 are the damping coefficients of the outer and inner masses, respectively. The equations of motion of the outer masses in the first and last unit cells are

$$\begin{cases} m_1\ddot{u}_1^{(1)} + k_1(2u_1^{(1)} - u_0 - u_1^{(2)}) + c_1(2\dot{u}_1^{(1)} - \dot{u}_0 - \dot{u}_1^{(2)}) + k_2(u_1^{(1)} - u_2^{(1)}) + c_2(\dot{u}_1^{(1)} - \dot{u}_2^{(1)}) = 0, \\ m_1\ddot{u}_1^{(n)} + k_1(2u_1^{(n)} - u_1^{(n-1)}) + c_1(2\dot{u}_1^{(n)} - \dot{u}_1^{(n-1)}) + k_2(u_1^{(n)} - u_2^{(n)}) + c_2(\dot{u}_1^{(n)} - \dot{u}_2^{(n)}) = 0. \end{cases} \tag{9}$$

Applying the Laplace transform to Eqs. (8) and (9), and replacing u_2 with u_1, one can obtain

$$\begin{cases} (k_1 + i\omega c_1)U_0 - \left(-\omega^2 m_1 + 2k_1 + 2i\omega c_1 + k_2 + i\omega c_2 - \dfrac{(k_2 + i\omega c_2)^2}{k_2 + i\omega c_2 - \omega^2 m_1}\right)U_1^{(1)} + (k_1 + i\omega c_1)U_1^{(2)} = 0, \\ (k_1 + i\omega c_1)U_1^{(j-1)} - \left(-\omega^2 m_1 + 2k_1 + 2i\omega c_1 + k_2 + i\omega c_2 - \dfrac{(k_2 + i\omega c_2)^2}{k_2 + i\omega c_2 - \omega^2 m_1}\right)U_1^{(j)} + (k_1 + i\omega c_1)U_1^{(j+1)} = 0, \\ (k_1 + i\omega c_1)U_1^{(n-1)} - \left(-\omega^2 m_1 + k_1 + i\omega c_1 + k_2 + i\omega c_2 - \dfrac{(k_2 + i\omega c_2)^2}{k_2 + i\omega c_2 - \omega^2 m_1}\right)U_1^{(n)} = 0, \end{cases} \tag{10}$$

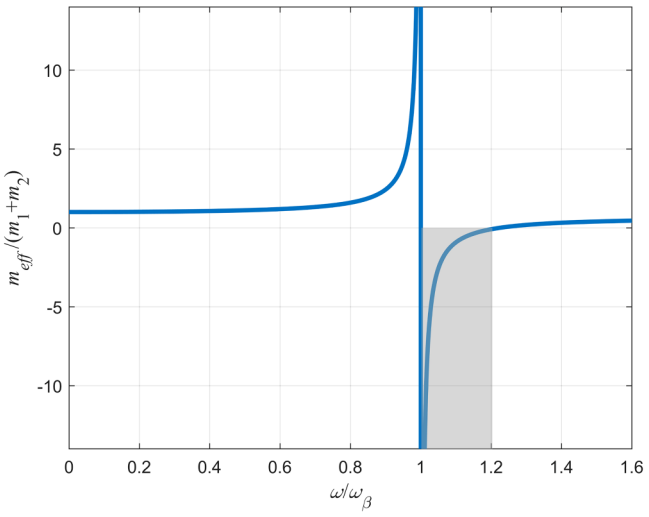

FIG. 3. Dimensionless effective mass vs ω/ω_β of a unit cell of conventional lattice metamaterial system.

where U_0 and U_1 denote the magnitudes of displacements of the base excitation and an outer mass, respectively. Through iterative substitution, one can acquire the transmittance of the conventional finite lattice model, which is defined by

$$T = 20\log_{10}\left|\frac{U_1^{(n)}}{U_0}\right|. \tag{11}$$

Figure 5 plots the transmittance of the conventional finite lattice metamaterial system consisting of eight unit cells with the mass and stiffness parameters $m_1 = 0.05$ kg, $m_2 = 0.025$ kg, $k_1 = 50$ N/m, and $k_2 = 60$ N/m as before and damping coefficients $c_1 = c_2 = 0.004$ N s/m. The bandgap prediction from the analytical expression Eq. (6) is shaded in blue, which is in good agreement with the vibration attenuation region (the deep valley) in the transmittance. Meanwhile, it can be found that the bandgap prediction based on negative effective mass [Eq. (7)] shaded in red does not match the bandgap observed from the transmittance, that is, the bandgap does not start from the natural frequency of the local resonator ω_β but from the frequency corresponding to a large positive effective mass m_{eff}. A more detailed explanation of this conclusion can be seen in Ref. 34.

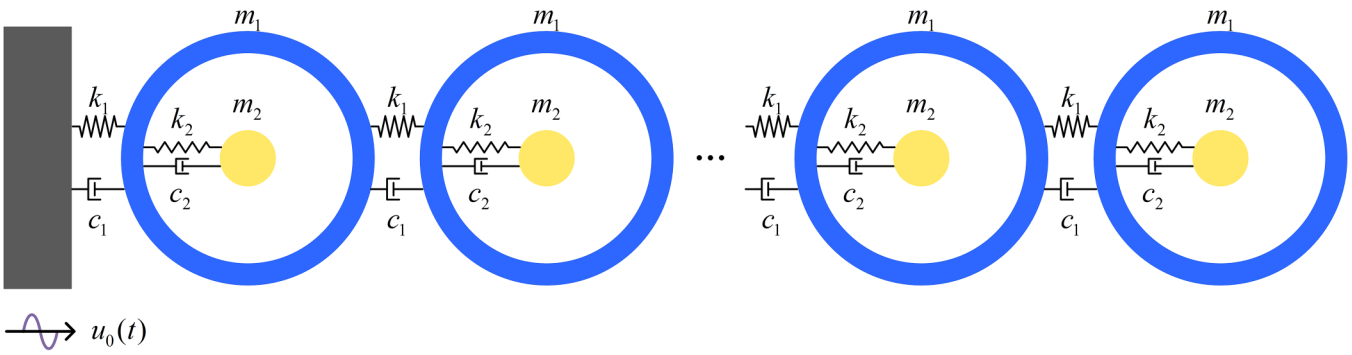

FIG. 4. Conventional finite lattice metamaterial system.

B. Estimation of bandgap bounds of metabeam with mechanical local resonators

In the following subsections II B, II C, and II D, the proposed approach will be applied to several typical metabeams. The representative schematic of a conventional metabeam that consists of a host beam and an array of periodically attached mechanical local resonators is shown in Fig. 6. Based on Euler's beam theory, the partial differential equation that governs the transverse elastic wave propagation in the unit cell can be written as

$$E_b I_b \frac{\partial^4 w(x,t)}{\partial x^4} + M\frac{\partial^2 w(x,t)}{\partial t^2} - k(u(x,t) - w(x,t))\delta(x) = 0, \quad (12)$$

where $w(x, t)$ is the transverse displacement of the beam and $u(x, t)$ is the displacement of the local resonator. $\delta(x)$ is the Dirac delta function. E_b and I_b represent Young's modulus and the area moment of inertia of the host beam, respectively. $M = \rho_b \times A_b$ is the mass per unit length with ρ_b being the density and $A_b = b \times h_b$ being the cross-sectional area of the host beam. b and h_b are the width and thickness of the host beam, respectively. The motion of the local resonator is governed by

$$\left(m\frac{\partial^2 u(x,t)}{\partial t^2} + k(u(x,t) - w(x,t))\right)\delta(x) = 0, \quad (13)$$

where m and k are the mass and stiffness of the local resonator, respectively. For this infinitely periodic structure, the time-harmonic solutions of $w(x, t)$ and $u(x, t)$ satisfy the following forms according to Bloch's theorem,

$$w(x,t) = We^{i(qx-\omega t)},\ u(x,t) = Ue^{i(qx-\omega t)}. \quad (14)$$

W and U are the amplitudes of the displacements of the propagating wave and the local resonator, respectively. To obtain a concise dispersion equation, we made a homogenization assumption to simplify the model. By considering the beam as a homogenous uniform beam, one can derive the dynamic characteristic of this periodic structure by substituting Eq. (14) into (12) and (13) and integrating (12) and (13) over the cell length from $-d/2$ to $d/2$. The result is rearranged in the matrix form as

$$\begin{bmatrix} 2q^3 E_b I_b \sin\left(\frac{dq}{2}\right) - \frac{2\omega^2}{q} M \sin\left(\frac{dq}{2}\right) + k & -k \\ -k & k - m\omega^2 \end{bmatrix} \begin{bmatrix} W \\ U \end{bmatrix} = \begin{bmatrix} 0 \\ 0 \end{bmatrix}. \quad (15)$$

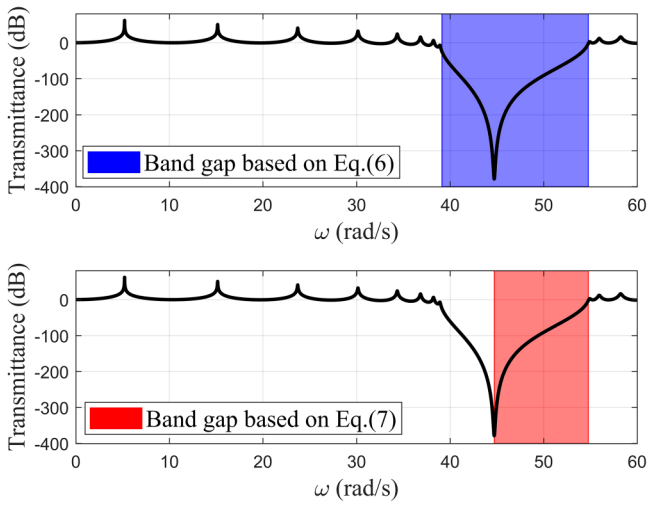

FIG. 5. Transmittance of conventional finite lattice metamaterial system with eight unit cells superposed with bandgap predictions from bound expressions [results of Eqs. (6) and (7) are shaded in blue and red, respectively].

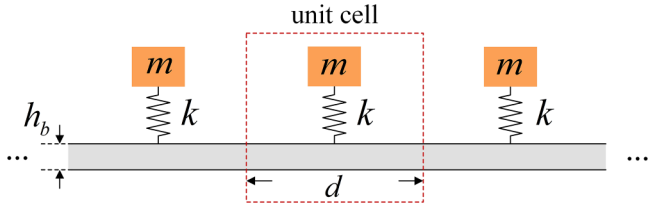

FIG. 6. Metabeam with mechanical local resonators.

To ensure the existence of non-trivial solutions, the coefficient matrix of Eq. (15) should be zero. Therefore, the characteristic equation (i.e., the dispersion equation) of the unit cell is obtained as

$$f(\omega,q)=\frac{2mM\sin\left(\frac{dq}{2}\right)}{q}\omega^4-\frac{kmq+(2kM+2E_bI_bmq^4)\sin\left(\frac{dq}{2}\right)}{q}\omega^2+2E_bI_bkq^3\sin\left(\frac{dq}{2}\right)=0. \tag{16}$$

For this quartic equation, there are at least two real roots $\omega_n(q)$, $n=1,2$ as shown below,

$$\omega_n(q)=\sqrt{(-1)^{n-1}\sqrt{B}+\frac{kq}{4M\sin\left(\frac{dq}{2}\right)}+\frac{k}{2m}+\frac{E_bI_bq^4}{2M}}, \tag{17}$$

where

$$B=\frac{k^2}{4m^2}+\frac{k^2q^2}{16M^2\sin^2\left(\frac{dq}{2}\right)}+\frac{(E_bI_b)^2q^8}{4M^2}+\frac{k^2q}{4mM\sin\left(\frac{dq}{2}\right)}+\frac{E_bI_bkq^5}{4M^2\sin\left(\frac{dq}{2}\right)}-\frac{E_bI_bkq^4}{2mM}$$

and $n=1,2$ denote the r_u and r_l curves. The following content in this subsection is to derive the bandgap bound equations based on the extreme point theory mentioned in Subsection II A. Since the direct derivative of Eq. (17) would result in a lengthy expression, here we take an implicit function derivative of Eq. (16), which yields

$$\frac{d\omega}{dq}=-\frac{f'_q}{f'_\omega}=\frac{A_1\omega^4+A_2\omega^2+6E_bI_bkq^4\sin\left(\frac{dq}{2}\right)+E_bI_bdkq^5\cos\left(\frac{dq}{2}\right)}{-8mqM\sin\left(\frac{dq}{2}\right)\omega^3+\left(2kmq^2+4(kqM+E_bI_bmq^5)\sin\left(\frac{dq}{2}\right)\right)\omega}, \tag{18}$$

where

$$A_1=mqdM\cos\left(\frac{dq}{2}\right)-2mM\sin\left(\frac{dq}{2}\right),$$

$$A_2=(2kM-6E_bI_bmq^4)\sin\left(\frac{dq}{2}\right)-(dkqM+E_bI_bdmq^5)\cos\left(\frac{dq}{2}\right),$$

and f'_q and f'_ω denote the partial derivatives of f with respect to q and ω, respectively. By setting Eq. (18) equal to zero, one root can be analytically solved through MATLAB's solve() function, which is

$$\omega_1^*=\omega_m, \tag{19}$$

where $\omega_m=\sqrt{\frac{k}{m}}$ denotes the natural frequency of the local resonator. The dispersion curves of the metabeam are very similar to those of the lattice metamaterial system in the first Brillouin zone (Fig. 1). ω_1^* can be further verified as the extreme point E1 of the r_l curve. However, with the implicit function derivative, the root related to the extreme point E2 of r_u curve is lost. From the band structure analysis in Sec. II A, E2 is located at $q=0$ in the r_u curve. Since q appears in the denominator of $\omega_1(q)$, E2 is evaluated by finding the limit of $\omega_1(q)$ when $q\to 0$,

$$\omega_2^*=\lim_{q\to 0}\omega_1(q). \tag{20}$$

Ignoring the high-order terms of q, one can reduce Eq. (20) to

$$\omega_2^*=\lim_{q\to 0}\left(\sqrt{k}\sqrt{\sqrt{\frac{1}{4m^2}+\frac{\lambda^2(q)}{16M^2}}+\frac{\lambda(q)}{4mM}}+\frac{\lambda(q)}{4M}+\frac{1}{2m}\right), \tag{21}$$

where $\lambda(q)=\frac{q}{\sin\left(\frac{dq}{2}\right)}$. Note that $\lim_{q\to 0}\lambda(q)=\frac{2}{d}$. By inserting this into Eq. (21), Eq. (20) is evaluated to be

$$\omega_2^*=\omega_m\sqrt{\mu+1}, \tag{22}$$

where $\mu=\frac{m}{Md}$is the mass ratio. Note that when $q\to 0$, we have $\sin\left(\frac{dq}{2}\right)\approx\frac{dq}{2}$. Inserting it into $\lim_{q\to 0}\left(\frac{d\omega}{dq}\right)$ and rearranging the equation leads to

$$\lim_{q\to 0}\left(\frac{d\omega}{dq}\right)=\frac{-4E_bI_bdm\omega^2+4E_bI_bdk}{(2E_bI_bdm\omega)q+(2km\omega(d+1)-4dmM\omega^3)q^{-3}}=0, \tag{23}$$

which means E2 is the extreme point of r_u. This confirms our assumption that the bandgap bounds are located at the extreme points of dispersion curves. The bandgap of the metabeam with

mechanical local resonators is thus determined to be in the frequency range

$$\omega_m < \omega < \omega_m\sqrt{\mu+1}, \tag{24}$$

and the bandgap width is

$$\Delta\omega = \left(\sqrt{\mu+1}-1\right)\omega_m. \tag{25}$$

It can be found that the bandgap begins from the natural frequency of the local resonator and is proportional to the mass ratio μ. Interestingly, this is different from the lattice system. This expression is consistent with what was obtained in Ref. 30 under the assumption of a finitely long beam with an infinite number of local resonators. In Subsections II C and II D, more beam-type continuous models will be presented to further examine the generality of the proposed bandgap estimation approach. The validation of bandgap bound expressions in this and Subsections II C and II D will be conducted using COMSOL in Sec. IV.

C. Estimation of bandgap bounds of piezoelectric metabeam with shunt resonant circuits

Figure 7 shows a piezoelectric metabeam with shunt resonant circuits. It consists of a host beam bonded with a pair of thin piezoelectric layers with the same poling directions. h_b and h_p denote the thicknesses of the host beam and piezoelectric layers, respectively, while b denotes their widths, which are assumed to be the same. The host beam is assumed to be made of metal that is grounded. Periodic electrode pairs are applied to the piezoelectric layers with a lattice constant d. The top and bottom piezoelectric layers in one unit cell are electrically connected in parallel with shunt resonant circuits, which have the same impedance Z. The constitutive equations of the piezoelectric layer are

$$\begin{bmatrix} T_1 \\ D_3 \end{bmatrix} = \begin{bmatrix} E_p & -e_{31} \\ e_{31} & \varepsilon_{33}^S \end{bmatrix} \begin{bmatrix} S_1 \\ E_3 \end{bmatrix}, \tag{26}$$

where S_1 and T_1 denote the strain and stress along the x direction and D_3 and E_3 denote the electric displacement and electric field along the z direction, respectively. E_p, e_{31}, and ε_{33}^S are the effective short circuit Young's modulus, effective piezoelectric stress constant, and effective permittivity component at constant strain, respectively. Under the plane-stress assumption in Ref. 35, one-dimensional (1D) effective material properties can be derived from the three-dimensional (3D) constitutive equations as follows:

$$E_p = \frac{1}{s_{11}^E}, e_{31} = \frac{d_{31}}{s_{11}^E}, \varepsilon_{33}^S = \varepsilon_{33}^T - \frac{d_{31}^2}{s_{11}^E}, \tag{27}$$

where s_{11}^E is the elastic compliance at constant electric field, d_{31} is the piezoelectric strain constant, and ε_{33}^T is the permittivity component at constant stress. With the parallel connection of piezoelectric layers, Young's modulus of the piezoelectric layer can be modified as[36]

$$E_{p,eff}(\omega) = E_p\left(1 - \frac{k_{31}^2}{1 + i\omega C_p^s Z(\omega)}\right), \tag{28}$$

where $C_p^s = \frac{2\varepsilon_{33}^S bd}{h_p}$ represents the inherent piezoelectric capacitance and $k_{31} = d_{31}\sqrt{\frac{1}{s_{11}^E \varepsilon_{33}^T}}$ is the electromechanical coupling coefficient.

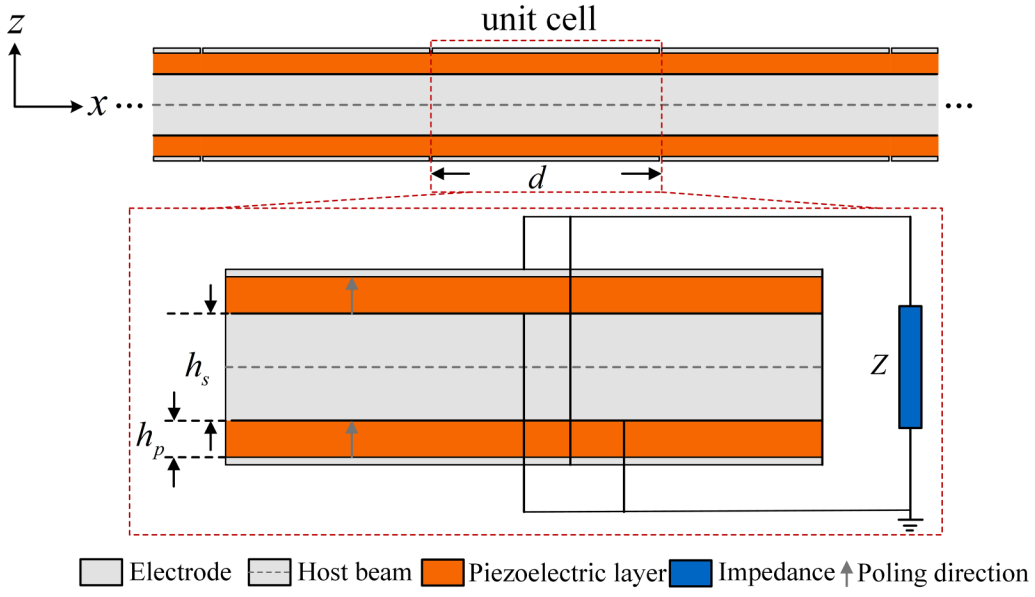

FIG. 7. Piezoelectric metabeam with shunt resonant circuits.

Since a pure inductor L is considered, the impedance of the connected shunt circuit is $Z(\omega) = i\omega L$. Based on Euler's beam theory, the governing electromechanical equation of the piezoelectric metabeam can be represented as

$$EI_{eff}(\omega)\frac{\partial^4 w}{\partial x^4} + M_{eff}\frac{\partial^2 w}{\partial t^2} = 0, \tag{29}$$

where the effective flexural rigidity EI_{eff} and the effective mass per length M_{eff} are

$$EI_{eff}(\omega) = E_b I_b + E_{p,eff}(\omega) I_p, \ \ldots, M_{eff} = \rho_b A_b + 2\rho_p A_p, \tag{30}$$

where $I_b = \frac{bh_b^3}{12}$, ρ_b, and A_b denote the second moment of inertia, density, and the cross-sectional area of the substrate, respectively, while $I_p = \frac{2b}{3}\left(\left(h_p + \frac{h_b}{2}\right)^3 - \frac{h_b^3}{8}\right)$, ρ_p, and $A_p = b \times h_p$ denote those of the piezoelectric layer. For this infinitely periodic structure, the solution of $w(x,t)$ satisfies the same form as Eq. (14) according to Bloch's theorem. By substituting Eq. (14) into (29) and integrating (29) over the cell length d, the dispersion equation of the electromechanical system is obtained as

$$f(\omega, q) = EI_{eff}(\omega)q^4 + M_{eff}\omega^2 = 0. \tag{31}$$

Substituting Eq. (28) into (30), one can obtain the two real roots from the quartic equation in Eq. (31),

$$\omega_n(q) = \sqrt{\frac{(-1)^n\sqrt{\beta_1^2 q^8 + 2(\beta_1 - 2\beta_2)M_{eff}q^4\omega_e + M_{eff}^2\omega_e^4} + \beta_1 q^4 + M_{eff}\omega_e^2}{2M_{eff}}} = 0,\ n = 1, 2, \tag{32}$$

where $\beta_1 = E_p I_p + E_b I_b$ and $\beta_2 = (1 - k_{31}^2)E_p I_p + E_b I_b$, which are actually the effective flexural rigidities in short circuit and open circuit conditions, respectively. $\omega_e = 1/\sqrt{LC_p^s}$ represents the natural frequency of the LC circuit. $n = 1, 2$ denote the r_l and r_u dispersion curves in the ω–q plane, respectively. Similarly, we explore the bandgap bound equations of this model based on the extreme point assumption. The derivative function of Eq. (31) can be obtained as

$$\frac{d\omega}{dq} = -\frac{f'_q}{f'_\omega} = \frac{-4(\beta_1\omega^2 - \beta_2\omega_e^2)q^3}{(2M_{eff}\omega_e^2 + 2\beta_1 q^4)\omega - 4M_{eff}\omega^3 + \frac{2(M_{eff}\omega^5 - (M_{eff}\omega_e^2 + \beta_1 q^4)\omega^3 + \beta_2 q^4\omega_e^2\omega)}{\omega^2 - \omega_e^2}}. \tag{33}$$

By setting $\frac{d\omega}{dq} = 0$, one root can be solved, which is identified as the lower bound of the bandgap,

$$\omega_1^* = \sqrt{\frac{\beta_2}{\beta_1}}\omega_e. \tag{34}$$

Also, the root related to the extreme point E2 of the r_u curve is lost by using the implicit function derivative. Since E2 is simply the intercept of the r_u curve, it can be evaluated by substituting $q = 0$ into $\omega_2(q)$ in Eq. (32), leading to

$$\omega_2^* = \omega_e. \tag{35}$$

Similar to Subsection II B, we can verify that it is the extreme point of the r_u curve by taking the limit of Eq. (33) at $q \to 0$, that is, $\lim_{q\to 0}\left(\frac{d\omega}{dq}\right)$. Note that the numerator of Eq. (33) is equal to zero, while the denominator of Eq. (33) is a constant, leading to $\lim_{q\to 0}\left(\frac{d\omega}{dq}\right) = 0$. Therefore, $\omega = \omega_e$ is the extreme point of the r_u curve, which is identified as the upper bound of the bandgap. The bandgap of the piezoelectric metabeam with shunt resonant circuits is thus located in the frequency range

$$\sqrt{\frac{\beta_2}{\beta_1}}\omega_e < \omega < \omega_e, \tag{36}$$

and the bandgap width is

$$\Delta\omega = \left(1 - \sqrt{\frac{\beta_2}{\beta_1}}\right)\omega_e. \tag{37}$$

Unlike the bandgap in metabeam with mechanical local resonators in Subsection II B [Eq. (24)], Eq. (36) implies that the upper bound of the bandgap of the piezoelectric metabeam is located at the natural frequency of the LC shunt circuit. The bandgap width depends on the coefficient $(1 - \sqrt{\beta_2/\beta_1})$, which is related to the electromechanical coupling coefficient k_{31} and the geometric properties. Additionally, it can be shown that the effective flexural rigidity $EI_{eff} = 0$ when $\omega = \sqrt{\beta_2/\beta_1}\omega_e$ and EI_{eff} becomes negative when ω further increases until ω is greater than ω_e. Consequently, the bandgap can be considered the frequency range where the effective rigidity of the piezoelectric metabeam is negative. It should be pointed out that Eq. (36) is similar but not consistent

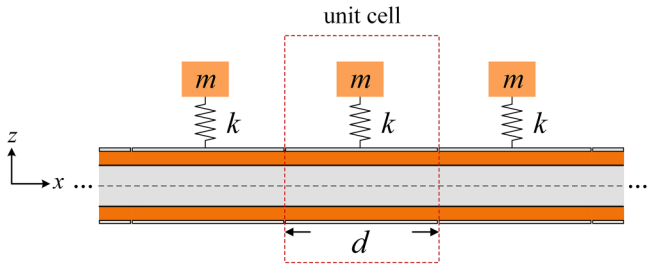

FIG. 8. Hybrid metabeam.

with the bound equation in Ref. 31,

$$\frac{1}{\sqrt{1+\dfrac{e_{31}^2 b h_p (h_b+h_p)^2}{2\beta_1 \varepsilon_{33}^S}}}\omega_e < \omega < \omega_e, \tag{38}$$

which was derived based on the assumption of infinite piezoelectric segments bonded onto a finitely long beam. Since there is a lack of finite element verification in Ref. 31, Eq. (36) will be compared with Eq. (38) later, as well as the results by the finite element method.

D. Estimation of bandgap bounds of a hybrid metabeam

To explore the fidelity of the proposed approach on estimating multiple bandgaps, a hybrid metabeam, which integrates the mechanical local resonators and piezoelectric shunt resonant circuits, is presented in this subsection (Fig. 8). By combining these two mechanisms, it is believed that two bandgaps could co-exist. The partial differential equation that governs the transverse elastic wave propagation in a unit cell of the hybrid metabeam can be written as

$$EI_{eff}\frac{\partial^4 w(x,t)}{\partial x^4} + M_{eff}\frac{\partial^2 w(x,t)}{\partial t^2} - k(u(x,t)-w(x,t))\delta(x) = 0\cdot \tag{39}$$

The motion of the local resonator is governed by

$$\left(m\frac{\partial^2 u(x,t)}{\partial t^2} + k(u(x,t)-w(x,t))\right)\delta(x) = 0. \tag{40}$$

For this infinitely periodic structure, the solutions of $w(x,t)$ and $u(x,t)$ satisfy the same forms as Eqs. (14) according to Bloch's theorem. Substituting Eqs. (14), (28), and (41) into Eqs. (39) and (40), integrating Eqs. (39) and (40) over the cell length, rearranging the equations in the matrix form and setting the determinant of the coefficient matrix to be zero, one can obtain the dispersion equation of the unit cell of the hybrid metabeam as

$$f(\omega,q) = \frac{2M_{eff}\sin\left(\dfrac{dq}{2}\right)\omega^6 + B_2\omega^4 + B_1\omega^2 + 2(k_{31}^2-2)E_pI_p\omega_m^2\omega_e^2 q^4 \sin\left(\dfrac{dq}{2}\right)}{q(\omega^2-\omega_e^2)} = 0, \tag{41}$$

where

$$B_1 = kq\omega_e^2 + 2M_{eff}\omega_m^2\omega_e^2\sin\left(\frac{dq}{2}\right) + 2(E_pI_p+E_bI_b)(\omega_m^2 + \omega_e^2)q^4\sin\left(\frac{dq}{2}\right) - 2E_pI_pk_{31}^2q^4\omega_e^2\sin\left(\frac{dq}{2}\right)$$

and

$$B_2 = -kq - 2(\omega_m^2+\omega_e^2)M_{eff}\sin\left(\frac{dq}{2}\right) - 2(E_pI_p+E_bI_b)q^4\sin\left(\frac{dq}{2}\right).$$

Similarly, three groups of positive real roots can be obtained by solving Eq. (41), which correspond to three dispersion curves, namely, r_l, r_m, and r_u, in the ω–q plane, where the subscript m denotes the middle curve. According to previous band structure analyses in Subsections II B and II C, four extreme points are expected to exist, which correspond to the upper and lower bounds of two bandgaps related to the mechanical local resonators and piezoelectric shunt resonant circuits, respectively. As discussed before, two extreme points can be determined by seeking the roots of the derivative function $\frac{d\omega}{dq} = -\frac{f'_q}{f'_\omega} = 0$, while the rest at the discontinuous point $q = 0$ can be obtained by following the same procedure in Subsections II B and II C for evaluating the limits of dispersion curves when $q \to 0$. The repetitive derivation is avoided, and the final expressions for the bandgap bounds can be obtained as

$$\omega_1^* = \omega_m,\ \ \omega_2^* = \omega_m\sqrt{\tilde{\mu}+1},\ \ \omega_3^* = \sqrt{\frac{\beta_2}{\beta_1}}\omega_e,\ \ \omega_4^* = \omega_e, \tag{42}$$

where $\tilde{\mu} = \frac{m}{M_{eff}d}$. It is noteworthy that the vibration attenuation effect from the two mechanisms of resonances will cancel each other in the overlap region, leading to the disappearance of the bandgap phenomenon. According to the width and location of the bandgaps of the mechanisms when they work alone, one can enumerate five types of bandgaps in the hybrid metabeam, which is simply a pairwise combination of the bounds in Eq. (42). For the ease of description, the bandgap due to the mechanical local resonators alone is termed as "MBG" and the bandgap due to the

piezoelectric shunt resonant circuits as "EBG." The five types of two bandgaps of the hybrid metabeam are as follows:

Type 1: $\omega_1^*-\omega_2^*$, $\omega_3^*-\omega_4^*$, the two bandgaps are separated.
Type 2: $\omega_1^*-\omega_3^*$, $\omega_2^*-\omega_4^*$, the two bandgaps overlap, and MBG is below EBG.
Type 3: $\omega_3^*-\omega_1^*$, $\omega_4^*-\omega_2^*$, the two bandgaps overlap, and EBG is below MBG.
Type 4: $\omega_1^*-\omega_3^*$, $\omega_4^*-\omega_2^*$, the two bandgaps overlap, and MBG completely contains EBG.
Type 5: $\omega_3^*-\omega_1^*$, $\omega_2^*-\omega_4^*$, the two bandgaps overlap, and EBG completely contains MBG.

In the case that the bandgaps are separated (i.e., type 1), due to two resonance mechanisms, the bandgap bound equations are

$$\omega_m < \omega < \omega_m\sqrt{\tilde{\mu}+1}, \tag{43}$$

$$\sqrt{\frac{\beta_2}{\beta_1}}\omega_e < \omega < \omega_e, \tag{44}$$

and the total bandgap width is

$$\Delta\omega = \left(1-\sqrt{\beta_2/\beta_1}\right)\omega_e + \left(\sqrt{\tilde{\mu}+1}-1\right)\omega_m. \tag{45}$$

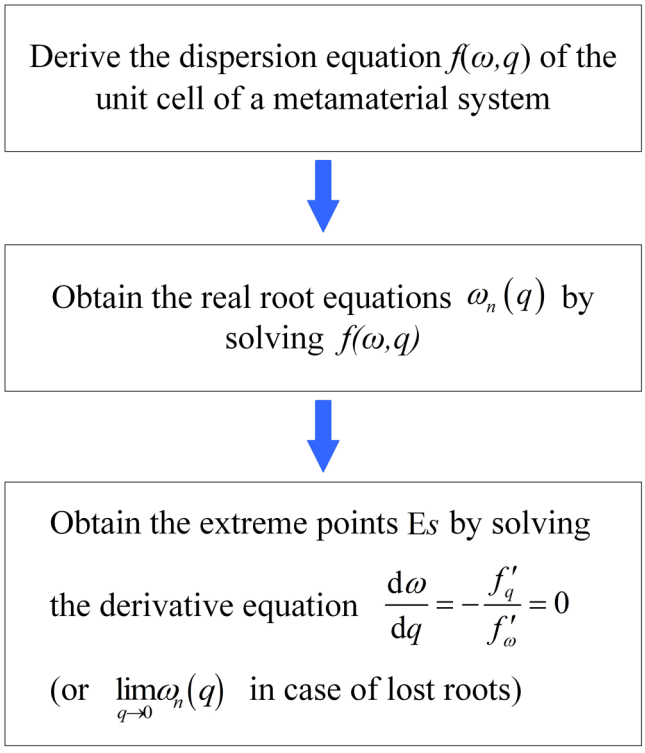

FIG. 9. A general procedure of determining the bandgap bounds of a metamaterial system based on the proposed approach.

It should be noted that the term $(1-\sqrt{\beta_2/\beta_1})$ is proportional to the thickness h_p, while the term $(\sqrt{\tilde{\mu}+1}-1)$ is inversely proportional to h_p. The influence of h_p on the total bandgap width will be discussed later. In summary, a general procedure of determining the bandgap bounds of a metamaterial system based on the proposed approach has been illustrated in Fig. 9.

III. FINITE ELEMENT ANALYSIS

The band structure and transmittance of the three metabeam models presented in Subsections II B–II D are analyzed using COMSOL for validation. Since only bending vibration is of interest, two-dimensional (2D) finite element (FE) models are established.

A. Band structure analysis

Figure 10(a) illustrates the FE model of a unit cell of the infinitely long metabeam with mechanical local resonators for band structure analysis. A lumped mass-spring element is attached to the center of the upper surface. The FE model of a unit cell of the infinitely long piezoelectric metabeam with shunt resonant circuits is shown in Fig. 10(b). The electrodes are implemented by applying terminal boundary conditions to the top surface of the upper piezoelectric layer and the bottom surface of the lower one. The other two surfaces of piezoelectric layers are grounded. The inductor is connected to the two electrode terminals by coupling their voltages. A commonly used piezoelectric ceramic material PZT-5H is assigned to the piezoelectric layer. Since the 3D piezoelectric constitutive equation is reduced to the 1D equation [Eq. (27)], modifications need to be made by setting the relative permittivity ε_{33}^S to be isotropic and letting the electromechanical coupling matrix be $\begin{bmatrix} 0 & 0 & 0 & 0 & 0 & 0 \\ 0 & 0 & 0 & 0 & 0 & 0 \\ e_{31} & 0 & 0 & 0 & 0 & 0 \end{bmatrix}$. The values of ε_{33}^S and e_{31} are calculated according to Eq. (27). Figure 10(c) shows the FE model of the infinitely long hybrid metabeam. Periodic constraints based on

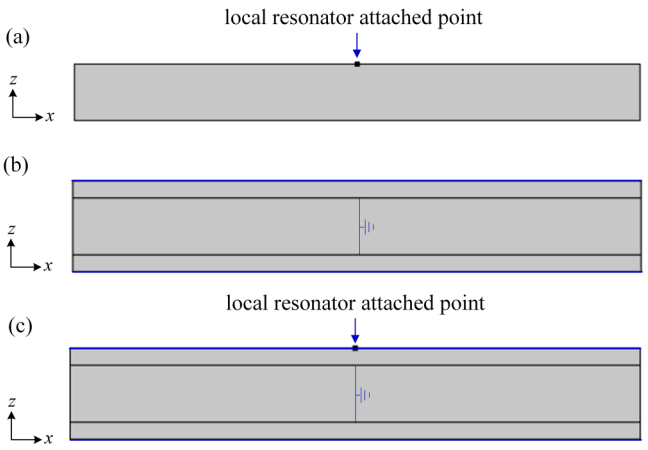

FIG. 10. Infinitely long FE models of various metabeams: (a) metabeam with mechanical resonators, (b) piezoelectric metabeam with shunt resonant circuits, and (c) hybrid metabeam.

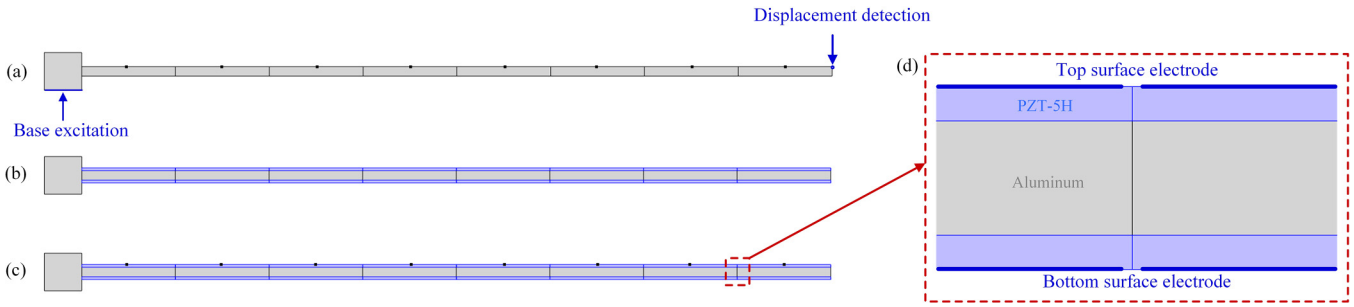

FIG. 11. Finitely long FE models of (a) metabeam with mechanical local resonators, (b) piezoelectric metabeam with shunt resonant circuits, and (c) hybrid metabeam with a close-up view near cell boundary shown in (d).

Eq. (14) are applied to the left and right bounds of the above three FE models.

B. Transmittance analysis

The FE models of the aforementioned three types of metabeams consisting of eight unit cells are shown in Figs. 11(a)–11(c). It is worth mentioning that the contact of the electrodes of adjacent unit cells will lead to a short circuit. Hence, a tiny area near the cell bound is deliberately selected to avoid applying the terminal boundary condition, as shown in Fig. 11(d). A displacement excitation is applied to the base and the transmittance can be calculated by detecting the displacement magnitude at the tip of the metabeam.

IV. VALIDATION

Table I lists the material and geometric parameters of the host beam (or substrate) and the piezoelectric layers. Specifically, it is well known that the Euler beam theory is only applicable for slender beams. Therefore, by referring to the parameters used in previous literature,[32] a small thickness to length ratio is considered in the following validation, which is 0.0125 for metabeam with mechanical local resonators and 0.02 for piezoelectric metabeam/hybrid metabeam, which can be calculated based on the parameters in Table I. The parameters of the mechanical resonators and shunt resonant circuit will be provided in Subsections IV A–IV C.

TABLE I. Material and geometric parameters used in the metabeams with eight unit cells.

Host beam (or substrate)	
Material	Aluminum
Density ρ_b	2700 kg/m^3
Young's modulus E_b	69 GPa
Dimensions in a unit cell	$10 \times 10 \times 1$ mm^3
Piezoelectric layer	
Material	PZT-5H
Young's modulus in short circuit E_p	60.6 GPa
Density ρ_p	7500 kg/m^3
Piezoelectric coefficient e_{31}	-16.61 C/m^2
Permittivity ε_{33}^S	2.5554×10^{-8} F/m
Dimensions in a unit cell	$10 \times 10 \times 0.3$ mm^3

A. Metabeam with mechanical local resonators

The FE results of the band structure and the transmittance of the metabeam with mechanical local resonators and their comparison with the theoretical estimation of the bandgap are shown in Figs. 12 and 13, respectively. The mass and spring stiffness of the resonator are $m_0 = 3 \times 10^{-4}$ kg and $k_0 = 5803.3$ N/m, so that the natural frequency of the mechanical local resonator is $f_m = 700$ Hz. As expected, the vibration attenuation region begins from f_m. It can be found that the bounds of the bandgap estimated by Eq. (24) are consistent with those observed from the FE result. Figure 14 further compares the FE result (bandgap observed from the band structure) and the theoretical estimation with different spring stiffnesses of the local resonators. Here, the dimensionless spring

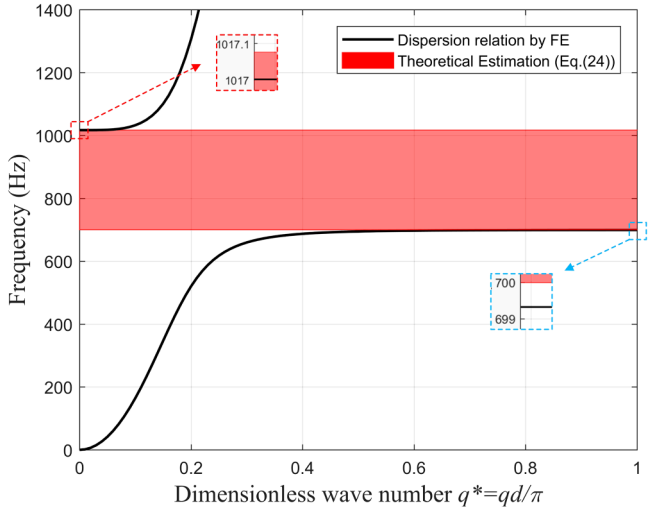

FIG. 12. Comparison of the theoretical estimation of bandgap and FE result of the band structure of metabeam with mechanical local resonators.

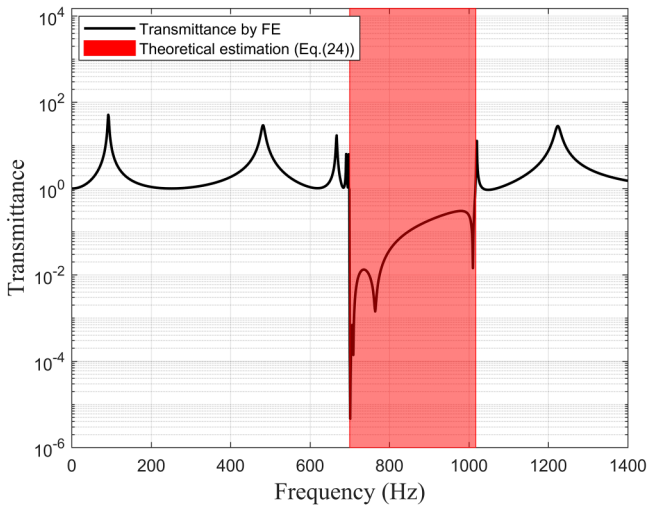

FIG. 13. Comparison of the theoretical estimation of bandgap and FE result of the transmittance of metabeam with mechanical local resonators.

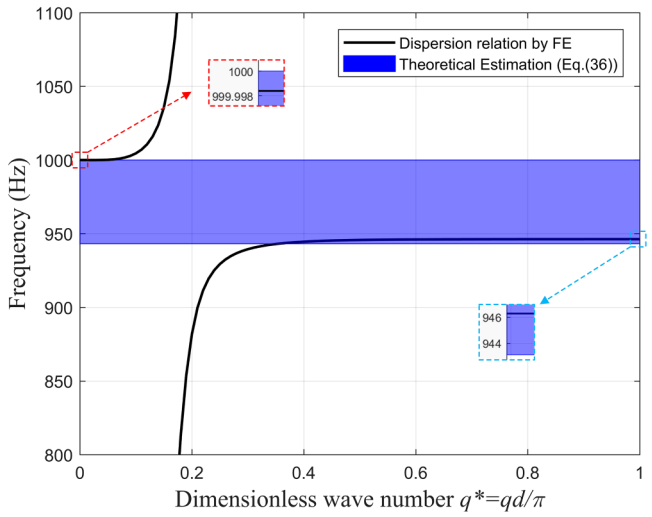

FIG. 15. Comparison of the theoretical estimation of bandgap and FE result of the band structure of piezoelectric metabeam with shunt resonant circuits.

stiffness $k^* = k/k_0$ is used. The relative error defined by $|f_{FE} - f_t|/f_{FE}$ is also plotted in Fig. 14, where f_{FE} and f_t are the FE and theoretical estimations of the bound frequencies, respectively. It illustrates that below the frequency of 3 kHz, the FE and theoretical results match well with relative errors <1%. With the increase of the spring stiffness of the local resonator, the discrepancy increases. The homogenous assumption in the modeling stage may cause the error. Under this assumption, the general wave solution is considered to be the same as that of a plain beam. In other words, the influence of the discontinuities caused by the reaction forces generated by the local resonators is not reflected in the wave function. With the increase of the spring stiffness, bandgap will shift to a higher frequency range, and the effect of discrete concentrated forces on the beam vibration pattern becomes more significant, leading to the increased discrepancy.

B. Piezoelectric metabeam with shunt resonant circuits

The FE results of the band structure and transmittance of the piezoelectric metabeam with shunt resonant circuits and their comparison with the theoretical estimation of the bandgap are shown

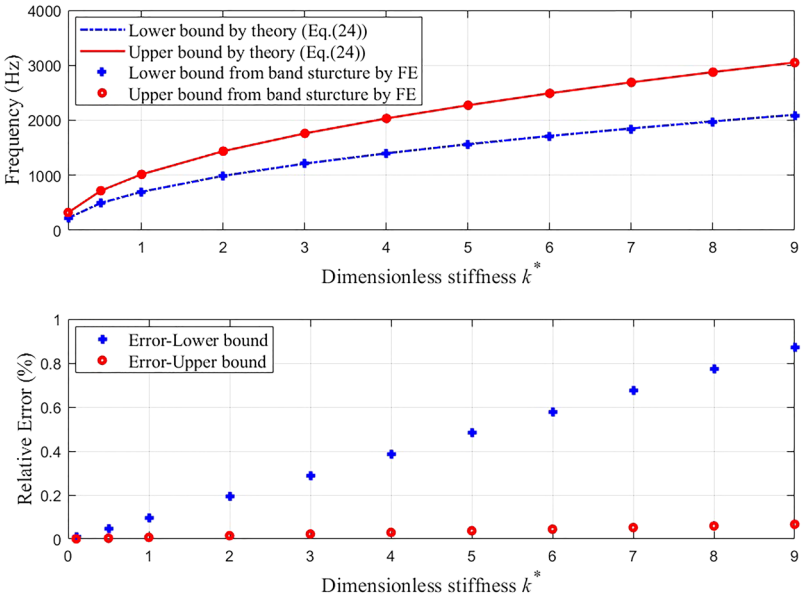

FIG. 14. Comparison of the theoretical and FE estimations of the lower and upper bounds of the bandgap of the metabeam with mechanical local resonators given different dimensionless spring stiffness k^*.

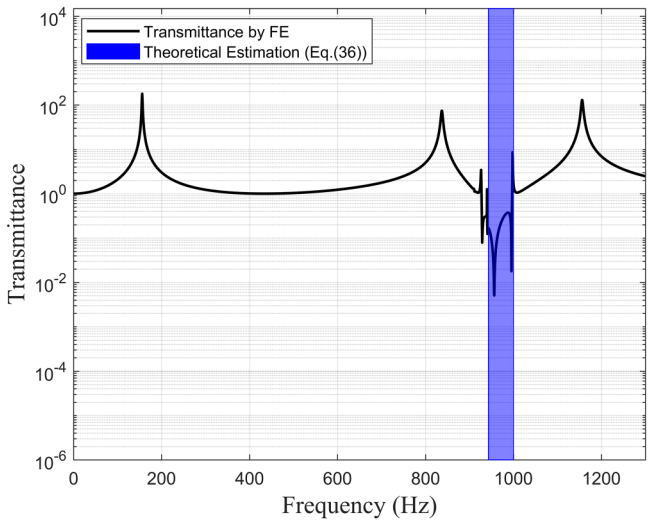

FIG. 16. Comparison of theoretical estimation of bandgap and FE result of the transmittance of the piezoelectric metabeam with shunt resonant circuits.

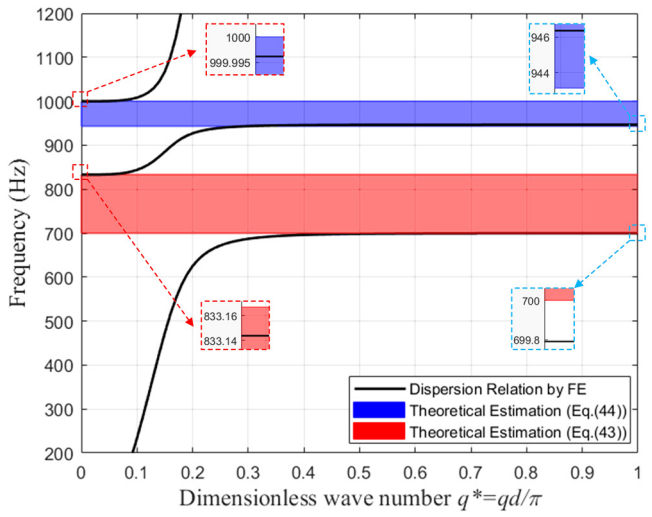

FIG. 18. Comparison of the theoretical estimation of bandgap and FE result of the band structure of the hybrid metabeam.

in Figs. 15 and 16, respectively. The inductor in the shunt resonant circuit is chosen to be $L_0 = 1.48$ H. With the parameters given in Table I, the internal capacitance of the piezoelectric layer C_p^s in the unit cell is 1.7×10^{-8} F, and the natural frequency of the shunt resonant circuit is $f_e = 1000$ Hz. Unlike that of the mechanical resonator based metabeam, the bandgap of the piezoelectric metabeam ends at the natural frequency of the shunt resonant circuit. The bandgap is estimated to be between 943.1–1000 Hz by Eq. (36), which agrees with observations from the FE results of the band structure and transmittance. To demonstrate the accuracy of Eq. (36), Fig. 17 compares the lower and upper bounds of the vibration attenuation region observed from the band structure by FE simulation and the theoretical estimation with the change of the inductive impedance L. Here, the dimensionless impedance $L^* = L/$

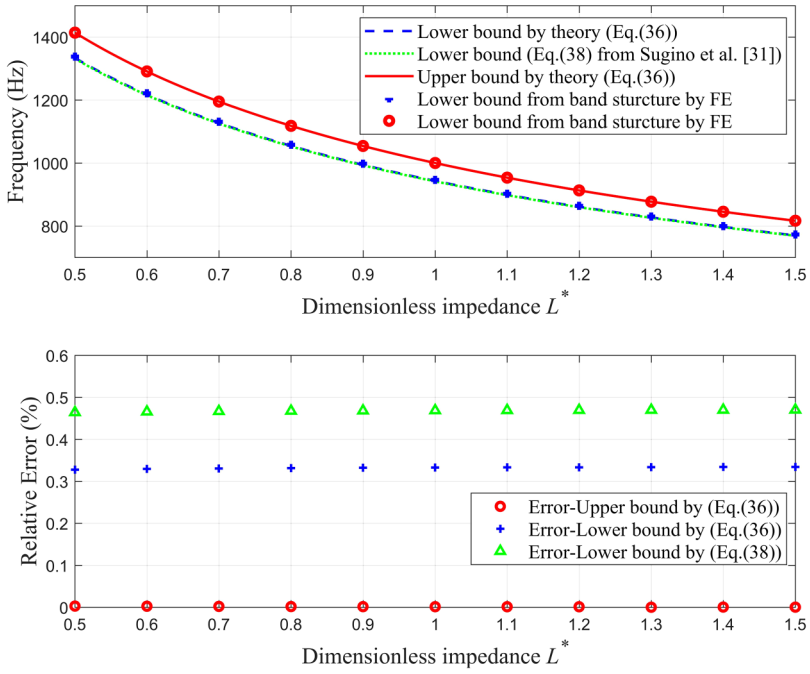

FIG. 17. Comparison of the theoretical and FE estimations of the lower and upper bounds of the bandgap of the piezoelectric metabeam given different dimensionless inductive impedance L^*. The prediction based on Eq. (38) from Sugino *et al.*[31] is also plotted for comparison.

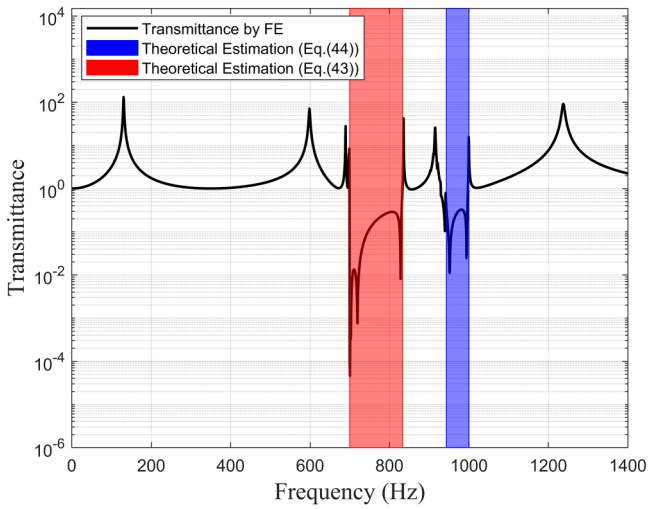

FIG. 19. Comparison of the theoretical estimation of bandgap and FE result of the transmittance of the hybrid metabeam.

L_0 is used. The theoretical estimation given by Eq. (38) from Sugino *et al.*[31] is also plotted in a green dotted line for comparison. With the increase of the inductance, the relative error of the prediction of bounds remains within 0.4%. Moreover, the bandgap bound equations derived based on the assumption of a finitely long beam carrying infinite piezoelectric segments shunted to resonant circuits[31] show slightly higher discrepancy than the FE result.

C. Hybrid metabeam

Using the same parameters in Subsections IV A and IV B, Figs. 18 and 19 show the FE results of the hybrid metabeam. Also, the corresponding bandgap regions predicted based on Eqs. (43) and (44) are superposed for comparison. To clearly show the evolution of error in a wider frequency range, Fig. 20 compares the lower and upper bounds of the bandgaps observed from the band structure by FE and theoretical estimation with varying k^* and L^*. Again, the theoretical predictions agree well with the FE results, with the relative errors of the estimations of the four bandgap bounds remaining below 1%.

V. FURTHER DISCUSSION

In Sec. IV, the derived expressions of bandgap bounds have been verified. Those expressions indicate the relationships between system parameters and the bandgap widths. Subsections V A and V B discuss the merits of the proposed theoretical approach for tailoring and optimization of the bandgap. An extended case is provided in Subsection V C to further demonstrate that this approach can be easily applied to more complicated metabeam systems.

A. Effect of m and h_p in a hybrid metabeam

In this section, we examine the effects of the mass of a mechanical local resonator m and the thickness of the piezoelectric

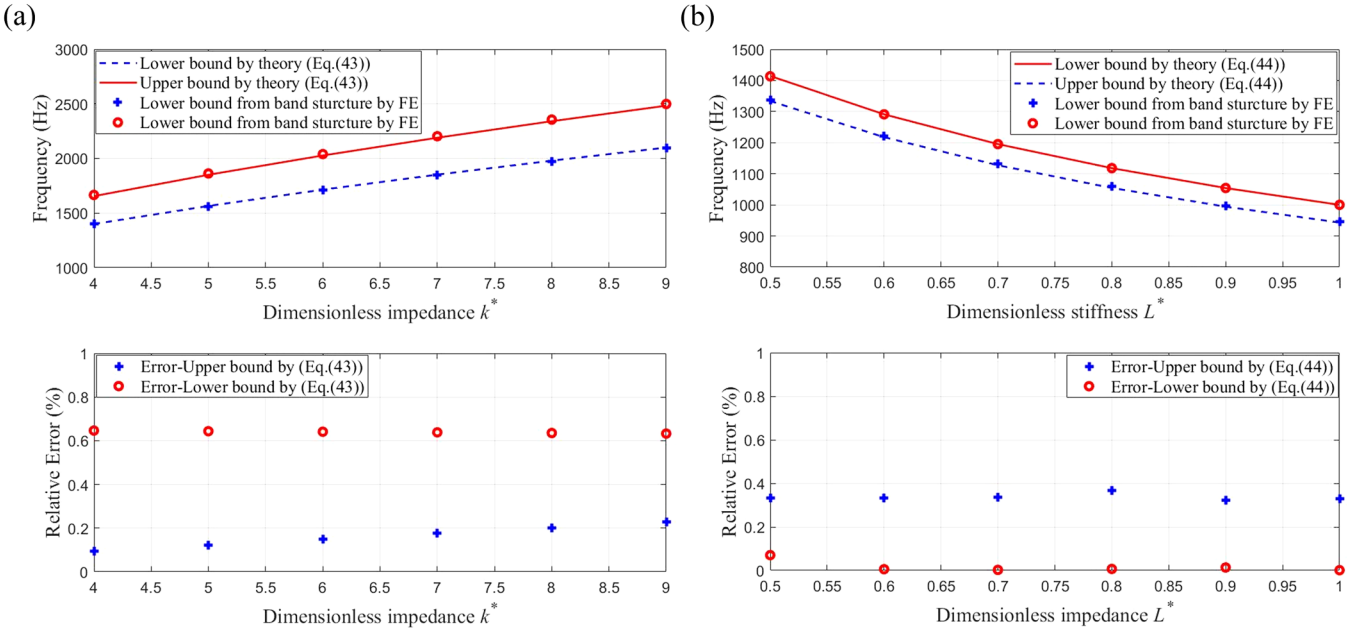

FIG. 20. Comparison of the theoretical and FE estimations of the lower and upper bounds of the two bandgaps of the hybrid metabeam: (a) MBG with L_0 and different dimensionless spring stiffness k^*; (b) EBG with k_0 and different dimensionless inductive impedance L^*.

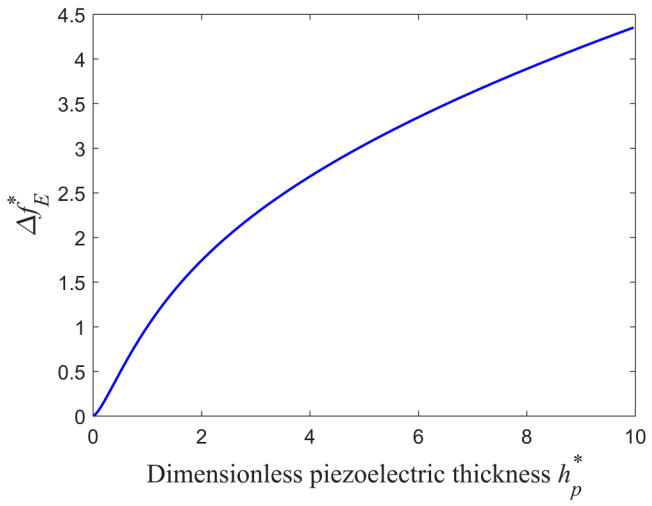

FIG. 21. Dimensionless EBG width Δf_E^* vs the dimensionless piezoelectric thickness h_p* of the hybrid metabeam.

layer h_p on the total bandgap width of the hybrid metabeam (denoted as "HBG"). The mechanical parameters of the mechanical local resonators and parameters of the shunt resonant circuits are fixed to be the same as those in Sec. IV ($k_0 = 5803.3$ N/m and $L_0 = 1.48$ H). The rest of the geometric and material parameters are listed in Table I.

Based on the second term of Eq. (45), the width of MBG in the hybrid metabeam increases monotonically with the unit-level mass ratio $\tilde{\mu}$. Furthermore, $\tilde{\mu}$ is proportional to m and decreases monotonically with h_p since $\tilde{\mu} = \frac{m}{M_{eff}d}$ and $M_{eff} = \rho_b h_s b + 2\rho_p h_p b$. Meanwhile, the width of EBG in the hybrid metabeam depends on $(1 - \sqrt{\beta_2/\beta_1})$ according to the first term of Eq. (45), which is influenced by h_p. As shown in Fig. 21, the increase of h_p* will lead to the increase of EBG Δf_E^*. Here $\Delta f_E^* = \Delta f_E/\Delta f_{E,0}$ is the dimensionless width of EBG and $h_p^* = h_p/h_{p,0}$ is the dimensionless thickness of the piezoelectric layer, where $h_{p,0} = 0.3$ mm. $\Delta f_{E,0} = 58.9$ Hz is the EBG of the hybrid metabeam with the parameters of L_0 and $h_{p,0}$. In general, increasing h_p* will reduce the unit-level mass ratio $\tilde{\mu}$, leading to the shrinking of the MBG, but it contributes to the widening of EBG.

Figure 22(a) shows the dimensionless width of HBG $\Delta f^* = \Delta f_H/\Delta f_{H,0}$ with varying h_p* and dimensionless mass $m^* = m/m_0$, where $m_0 = 3 \times 10^{-4}$ kg^{-1}. $\Delta f_{H,0} = 190$ Hz is the HBG of the hybrid metabeam with the parameters of k_0, m_0, L_0, and $h_{p,0}$. It is noted that HBG tends to increase monotonically with an increase of h_p* when m^* is small. However, for a large mass m^*, HBG will decrease first and then increase with the increase of h_p*. This change is because when m^* is small (e.g., $m^* = 0.1$), EBG dominates the HBG. Increasing h_p* leads to a significant increase in EBG but a minor decrease in MBG, giving an overall increase in HBG. When m^* is large (e.g., $m^* = 1.5$), MBG is much larger than EBG for a small h_p*. Increasing h_p* leads to the increase in EBG, but it is less significant than the decrease in MBG, resulting in the overall decrease of HBG. As h_p* continues to increase, this trend will change when h_p* reaches a certain value ($h_p^* = 2.2$), after which the increase in EBG becomes more remarkable than the decrease in MBG, resulting in the overall increase in HBG. Hence, there is a trade-off in the choice of the thickness of the piezoelectric layer. On the other hand, one can observe a narrow trench (denoted in gray) in Fig. 22(a). This trench is caused by the overlap of MBG and EBG, leading to the disappearance of the bandgap effect. The

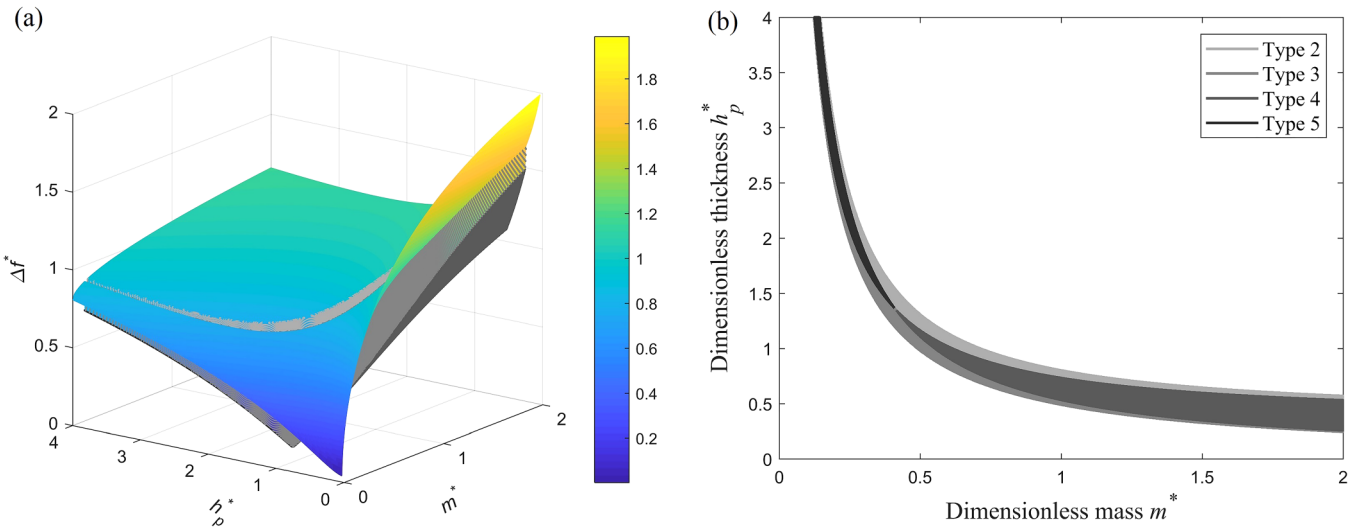

FIG. 22. (a) Dimensionless HBG width Δf^* vs the dimensionless piezoelectric thickness h_p* and the dimensionless mass of the mechanical local resonators m^* of the hybrid metabeam. (b) Four types of bandgaps of hybrid metabeam where MBG and EBG overlap.

locations of the four types of overlapped bandgaps (detailed descriptions in Subsection II D) are plotted with different gray scales in Fig. 22(b).

B. Tuning for aggregated bandgap of the hybrid metabeam

Since the expressions of the bounds of the two bandgaps of the hybrid metabeam have been obtained, it is theoretically possible to tune the two bandgaps to form a broad continuous vibration attenuation region by choosing suitable parameters. There are two ways to merge them:

(1) Let the jointing frequency be $\omega_j = \omega_m = \omega_e$. Then, the aggregated bandgap becomes $\sqrt{\beta_2/\beta_1}\omega_j < \omega < \sqrt{\tilde{\mu}+1}\omega_j$.
(2) Let the jointing frequency be $\omega_j = \sqrt{\beta_2/\beta_1}\omega_e = \sqrt{\tilde{\mu}+1}\omega_m$. Then, the aggregated bandgap becomes $\frac{1}{\sqrt{\tilde{\mu}+1}}\omega_j < \omega < \frac{1}{\sqrt{\beta_2/\beta_1}}\omega_j$.

The transmittances by FE for these two scenarios are shown in Figs. 23 and 24, respectively, in which one can observe the aggregated bandgap. In Fig. 23, the stiffness of the mechanical local resonator is changed to $k = 1.1844 \times 10^4$ N/m to ensure $f_j = f_m = f_e = 1000$ Hz. In Fig. 24, the stiffness of the mechanical local resonator is changed to $k = 7.4350 \times 10^3$ N/m to ensure $f_j = \sqrt{\beta_2/\beta_1}f_e = \sqrt{\tilde{\mu}+1}f_m = 943.13$ Hz. It should be pointed out that this combination is not perfect. A tiny peak exits near the adjacent point of the MBG and EBG. Since there exist minor discrepancies between FE and the derived expressions, MBG and EBG based on Eqs. (43) and (44) are not neatly jointed in the transmittance calculated by FE, which leads to minor overlap or separation of the MBG and EBG and consequently the tiny peak (a narrow passband) in the aggregated bandgap.

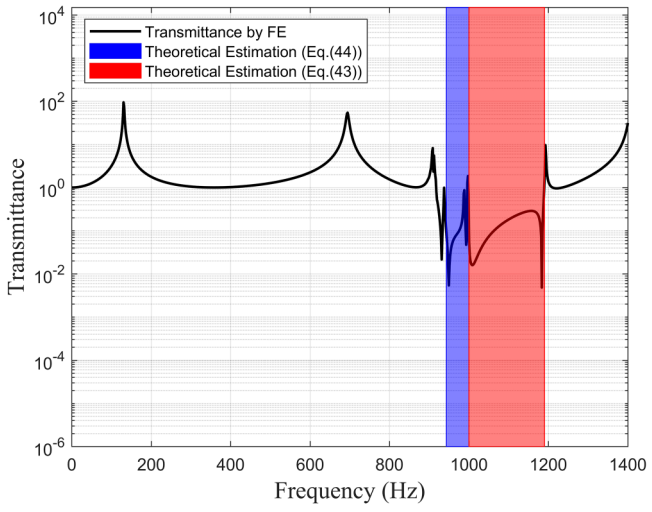

FIG. 23. Aggregated bandgap of hybrid metabeam observed from the transmittance by FE and the theoretical estimation with $f_j = f_m = f_e = 1000$ Hz.

C. An extended case

The bound estimation approach can be quickly applied to other metabeam systems. To demonstrate this, we further introduce a two-degree-of-freedom (2DOF) mechanical local resonator to the hybrid metabeam (Fig. 25). The bending vibration in the metabeam with multiple local resonators was comprehensively studied in Ref. 7. Similar to the concept in Ref. 7, with the multiple degrees of freedom in the mechanical local resonators, one can expect that an extra bandgap will appear in the configuration of Fig. 25 compared to the hybrid beam in Subsection V B. On the other hand, researchers explored the effect of nonlinear local resonators on the bandgap behavior. It was proved that introducing nonlinearities could potentially widen the bandgap. Interested readers can refer to Refs. 14 and 37.

Following a similar procedure in Sec. II, one can obtain the theoretical estimation of the bounds of the bandgaps and the steps are as follows:

(1) Derive the dispersion equation $f(\omega,q)$ of this hybrid metabeam with 2DOF local resonators. In this case, the equations of motion of the 2DOF local resonator are

$$\begin{cases} (m_1\ddot{u}_1(x,t) + k_1(u_1(x,t) - w(x,t)) + k_2(u_1(x,t) - u_2(x,t)))\delta(x) = 0, \\ (m_2\ddot{u}_2(x,t) + k_2(u_2(x,t) - u_1(x,t)))\delta(x) = 0, \end{cases} \tag{46}$$

where m_1 and m_2 are the masses in the local resonator; k_1 and k_2 represent the spring between the beam and m_1 and the spring between m_1 and m_2, respectively.
(2) Solve the derivative equation $\frac{d\omega}{dq} = -\frac{f'_q}{f'_\omega} = 0$, in which the roots associated with the lower bound of the bandgaps can be obtained.
(3) Evaluate the limits of dispersion curves when $q \to 0$ to obtain the upper bound of the bandgaps.

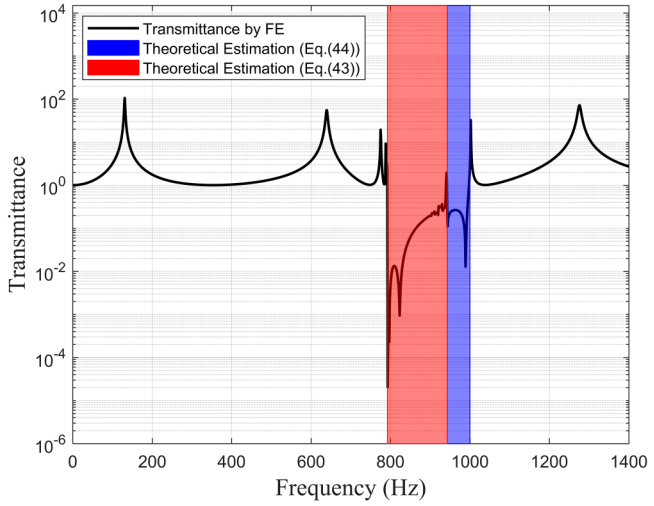

FIG. 24. Aggregated bandgap of hybrid metabeam observed from the transmittance by FE and the theoretical estimation with $f_j = \sqrt{\beta_2/\beta_1}f_e = \sqrt{\tilde{\mu}+1}f_m = 943.13$ Hz.

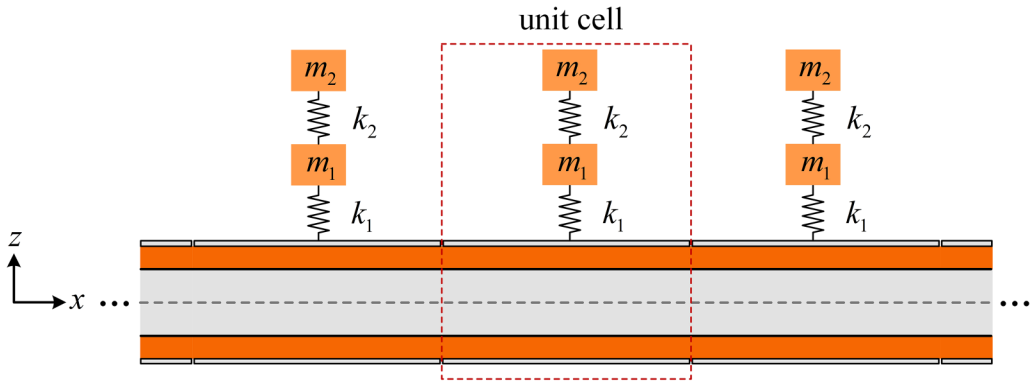

FIG. 25. Hybrid metabeam with 2DOF local resonators.

Without the detailed derivation for the sake of conciseness, the final derived bounds for the case that all the bandgaps (two MBGs and one EBG) are separated as follows:

The first bandgap generated by the 2DOF resonators:

$$\begin{cases} \omega_1^- = \dfrac{\sqrt{2}}{2}\sqrt{\omega_{m1}^2 + (\bar{\mu}_1 + 1)\omega_{m2}^2 - \sqrt{(\bar{\mu}_1\omega_{m2}^2 + (\omega_{m1} - \omega_{m2}))(\bar{\mu}_1\omega_{m2}^2 + (\omega_{m1} + \omega_{m2}))}}, \\ \omega_1^+ = \dfrac{\sqrt{2}}{2}\sqrt{(\bar{\mu}_2 + 1)\omega_{m1}^2 + (\bar{\mu}_1 + 1)\omega_{m2}^2 - \sqrt{C}}. \end{cases} \tag{47}$$

The second bandgap generated by the 2DOF resonators:

$$\begin{cases} \omega_2^- = \dfrac{\sqrt{2}}{2}\sqrt{\omega_{m1}^2 + (\bar{\mu}_1 + 1)\omega_{m2}^2 + \sqrt{(\bar{\mu}_1\omega_{m2}^2 + (\omega_{m1} - \omega_{m2},))(\bar{\mu}_1\omega_{m2}^2 + (\omega_{m1} + \omega_{m2}))}} \\ \omega_2^+ = \dfrac{\sqrt{2}}{2}\sqrt{(\bar{\mu}_2 + 1)\omega_{m1}^2 + (\bar{\mu}_1 + 1)\omega_{m2}^2 + \sqrt{C}}. \end{cases} \tag{48}$$

The bandgap generated by the shunt resonant circuits:

$$\begin{cases} \omega_3^- = \sqrt{\dfrac{\beta_2}{\beta_1}}\omega_e, \\ \omega_3^+ = \omega_e, \end{cases} \tag{49}$$

where

$$\bar{\mu}_1 = \frac{m_2}{m_1},\ \bar{\mu}_2 = \frac{m_1}{M_{eff}d},\ \omega_{m1} = \sqrt{\frac{k_1}{m_1}},\ \omega_{m2} = \sqrt{\frac{k_2}{m_2}},\ \omega_e = \sqrt{\frac{1}{C_p^s L}}$$

and

$$C = (\omega_{m1}^2 - \omega_{m2}^2)^2 + (\bar{\mu}_1^2 + 2\bar{\mu}_1)\omega_{m2}^4 + (\bar{\mu}_2^2 + 2\bar{\mu}_2)\omega_{m1}^4 + 2(\bar{\mu}_1 - \bar{\mu}_2 - \bar{\mu}_2\bar{\mu}_1)\omega_{m1}^2\omega_{m2}^2$$

Furthermore, a numeric example is provided to show an optimized design based on the derived analytical solutions [Eqs. (47)–(49)] and the three bandgaps are joined as an aggregated one. It is theoretically feasible to achieve this by properly choosing local resonator/shunt circuit parameters. One way to join these three bandgaps is as follows:

$$\begin{cases} \omega_1^+ = \omega_3^-, \\ \omega_2^- = \omega_3^+. \end{cases} \tag{50}$$

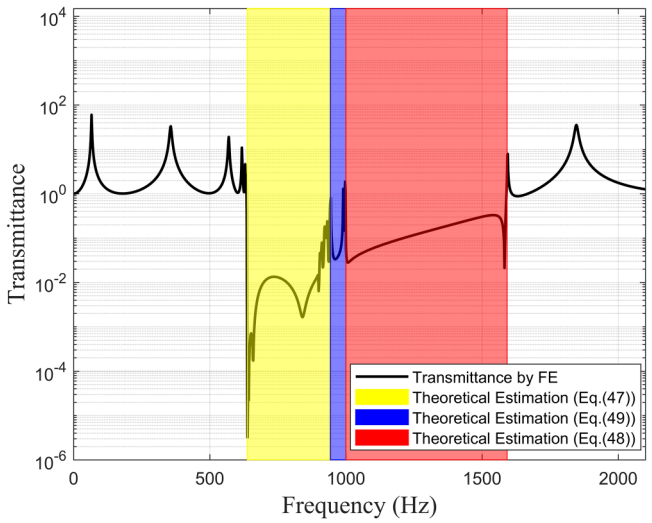

FIG. 26. The aggregated bandgap of hybrid metabeam with 2DOF local resonators observed from the transmittance by FE and the theoretical estimation.

Note that it is difficult to generate a bandgap with any intended width by tuning the LC shunt circuit. Therefore, we choose the inductance L to fix the bounds of EBG first. The geometric and material parameters are the same as those in Table I to avoid adding many new parameters. With $L = 1.48$ H, $f_e = \omega_e/2\pi = 1000$ Hz, $m_1 = 0.003$ /kg, and $m_2 = 0.0003$ /kg fixed, solving the simultaneous equations [Eq. (50)] can determine the stiffnesses of the 2DOF local resonators $k_1 = 5.7537 \times 10^4$ N/m and $k_2 = 9.9157 \times 10^3$ N/m, which gives the natural frequencies of $f_{m1} = \omega_{m1}/2\pi = 679$ Hz and $f_{m2} = \omega_{m2}/2\pi = 915$ Hz. Figure 26 shows the transmittance calculated by FE and the theoretical estimations of the bandgaps. This figure shows that the three bandgaps become an aggregated one with properly chosen parameters.

VI. CONCLUSIONS

In this paper, we have proposed a generic theoretical approach for fast estimating bandgap bounds of metamaterial beams. Based on wave equation, this approach is first developed and validated for the lattice system under the hypothesis that the extreme points of dispersion curves correspond to the bandgap bounds. By seeking the derivative of the dispersion equation, the closed-form expressions of bandgap bounds can be obtained straightforwardly. According to the verified expression by transmittance, the conjecture that the bandgap is associated with the frequency range where the effective mass is negative in the literature[33] is inappropriate for lattice systems. Subsequently, following the same general procedure, this approach is applied to three typical beam-type metamaterial systems and corresponding closed-form expressions of the bandgap bounds are derived. Specifically, the expression of the bandgap bounds of the mechanical resonators based metabeam is consistent with the well-known expression in the literature.[30] The expressions for the piezoelectric metabeam with shunt resonant circuits and the hybrid metabeam are slightly different from those in the literature.[22,31] Finite element models are also developed for both band structure and transmittance calculation, confirming that the derived expressions based on our proposed approach offer high accuracy. Based on the validated expressions, we further discuss the trade-off in the design of a hybrid metabeam to tailor the bandgaps and provide the guideline to form an aggregated bandgap. Furthermore, an extra case of hybrid metamaterial with 2DOF mechanical resonators is given to demonstrate the capability of this approach. In summary, the proposed approach in this work provides a powerful theoretical tool for estimating bandgap bounds and paves the way for the design and optimization of complicated metabeam systems.

ACKNOWLEDGMENTS

This work was financially supported by a Ph.D. scholarship from the China Scholarship Council (No. 201907000126) and the Faculty Research Development Fund from the University of Auckland (No. 3722094).

DATA AVAILABILITY

The data that support the findings of this study are available within the article.

REFERENCES

[1]S. Yao, X. Zhou, and G. Hu, "Experimental study on negative effective mass in a 1D mass–spring system," New J. Phys. **10**, 043020 (2008).
[2]Y. Ding, Z. Liu, C. Qiu, and J. Shi, "Metamaterial with simultaneously negative bulk modulus and mass density," Phys. Rev. Lett. **99**, 093904 (2007).
[3]P. A. Deymier, *Acoustic Metamaterials and Phononic Crystals* (Springer Science & Business Media, 2013).
[4]N. Gao, J. H. Wu, H. Hou, and L. Yu, "Excellent low-frequency sound absorption of radial membrane acoustic metamaterial," Int. J. Mod. Phys. B **31**, 1750011 (2017).
[5]L. Liu and M. I. Hussein, "Wave motion in periodic flexural beams and characterization of the transition between Bragg scattering and local resonance," J. Appl. Mech. **79**, 011003 (2012).
[6]Y. Achaoui, V. Laude, S. Benchabane, and A. Khelif, "Local resonances in phononic crystals and in random arrangements of pillars on a surface," J. Appl. Phys. **114**, 104503 (2013).
[7]R. Zhu, X. Liu, G. Hu, C. Sun, and G. Huang, "A chiral elastic metamaterial beam for broadband vibration suppression," J. Sound Vib. **333**, 2759–2773 (2014).
[8]H. Peng and P. Frank Pai, "Acoustic metamaterial plates for elastic wave absorption and structural vibration suppression," Int. J. Mech. Sci. **89**, 350–361 (2014).
[9]H. Chen, X. P. Li, Y. Y. Chen, and G. L. Huang, "Wave propagation and absorption of sandwich beams containing interior dissipative multi-resonators," Ultrasonics **76**, 99–108 (2017).
[10]G. Hu, L. Tang, and R. Das, "Internally coupled metamaterial beam for simultaneous vibration suppression and low frequency energy harvesting," J Appl. Phys. **123**, 055107 (2018).
[11]G. Huang and C. Sun, "Band gaps in a multiresonator acoustic metamaterial," J. Vib. Acoust. **132**, 031003 (2010).
[12]G. Hu, A. C. M. Austin, V. Sorokin, and L. Tang, "Metamaterial beam with graded local resonators for broadband vibration suppression," Mech. Syst. Signal Process. **146**, 106982 (2021).

[13]Y. Xiao, J. Wen, and X. Wen, "Broadband locally resonant beams containing multiple periodic arrays of attached resonators," Phys. Lett. A **376**, 1384–1390 (2012).
[14]W. Zhou, X. Li, Y. Wang, W. Chen, and G. Huang, "Spectro-spatial analysis of wave packet propagation in nonlinear acoustic metamaterials," J. Sound Vib. **413**, 250–269 (2018).
[15]J. Xu and R. Yan, "Exploitation of dimension-dependent behavior of piezoelectric metamaterial with LC shunt circuit," Eur. Phys. J. Appl. Phys. **83**, 20501 (2018).
[16]Y. Chen, G. Huang, and C. Sun, "Band gap control in an active elastic metamaterial with negative capacitance piezoelectric shunting," J. Vib. Acoust. **136**, 061008 (2014).
[17]G. Hu, J. Xu, L. Tang, C. Lan, and R. Das, "Tunable metamaterial beam using negative capacitor for local resonators coupling," J. Intell. Mater. Syst. Struct. **31**, 389–407 (2020).
[18]W. Zhou, Y. Wu, and L. Zuo, "Vibration and wave propagation attenuation for metamaterials by periodic piezoelectric arrays with high-order resonant circuit shunts," Smart Mater. Struct. **24**, 065021 (2015).
[19]G. Wang and S. Chen, "Large low-frequency vibration attenuation induced by arrays of piezoelectric patches shunted with amplifier–resonator feedback circuits," Smart Mater. Struct. **25**, 015004 (2015).
[20]X. Li, Y. Chen, G. Hu, and G. Huang, "A self-adaptive metamaterial beam with digitally controlled resonators for subwavelength broadband flexural wave attenuation," Smart Mater. Struct. **27**, 045015 (2018).
[21]G. Wang, J. Wang, S. Chen, and J. Wen, "Vibration attenuations induced by periodic arrays of piezoelectric patches connected by enhanced resonant shunting circuits," Smart Mater. Struct. **20**, 125019 (2011).
[22]C. Sugino, M. Ruzzene, and A. Erturk, "Merging mechanical and electromechanical bandgaps in locally resonant metamaterials and metastructures," J. Mech. Phys. Solids **116**, 323–333 (2018).
[23]Y. Chen, G. Hu, and G. Huang, "A hybrid elastic metamaterial with negative mass density and tunable bending stiffness," J. Mech. Phys. Solids **105**, 179–198 (2017).
[24]I.-L. Chang, Z.-X. Liang, H.-W. Kao, S.-H. Chang, and C.-Y. Yang, "The wave attenuation mechanism of the periodic local resonant metamaterial," J. Sound Vib. **412**, 349–359 (2018).
[25]D. Yu, Y. Liu, H. Zhao, G. Wang, and J. Qiu, "Flexural vibration band gaps in Euler-Bernoulli beams with locally resonant structures with two degrees of freedom," Phys. Rev. B **73**, 064301 (2006).
[26]H. Sun, X. Du, and P. F. Pai, "Theory of metamaterial beams for broadband vibration absorption," J. Intell. Mater. Syst. Struct. **21**, 1085–1101 (2010).
[27]P. Frank Pai, "Metamaterial-based broadband elastic wave absorber," J. Intell. Mater. Syst. Struct. **21**, 517–528 (2010).
[28]Y. Xiao, J. Wen, D. Yu, and X. Wen, "Flexural wave propagation in beams with periodically attached vibration absorbers: Band-gap behavior and band formation mechanisms," J. Sound Vib. **332**, 867–893 (2013).
[29]Y. Xiao, S. Wang, Y. Li, and J. Wen, "Closed-form bandgap design formulas for beam-type metastructures," Mech. Syst. Signal Process. **159**, 107777 (2021).
[30]C. Sugino, S. Leadenham, M. Ruzzene, and A. Erturk, "On the mechanism of bandgap formation in locally resonant finite elastic metamaterials," J. Appl. Phys. **120**, 134501 (2016).
[31]C. Sugino, M. Ruzzene, and A. Erturk, "Design and analysis of piezoelectric metamaterial beams with synthetic impedance shunt circuits," IEEE/ASME Trans. Mech. **23**, 2144–2155 (2018).
[32]C. Sugino, S. Leadenham, M. Ruzzene, and A. Erturk, "An investigation of electroelastic bandgap formation in locally resonant piezoelectric metastructures," Smart Mater. Struct. **26**, 055029 (2017).
[33]H. Huang, C. Sun, and G. Huang, "On the negative effective mass density in acoustic metamaterials," Int. J. Eng. Sci. **47**, 610–617 (2009).
[34]A. Banerjee, R. Das, and E. P. Calius, "Frequency graded 1D metamaterials: A study on the attenuation bands," J. Appl. Phys. **122**, 075101 (2017).
[35]A. Erturk and D. J. Inman, "A distributed parameter electromechanical model for cantilevered piezoelectric energy harvesters," J. Vib. Acoust. **130**, 041002 (2008).
[36]F. Casadei, T. Delpero, A. Bergamini, P. Ermanni, and M. Ruzzene, "Piezoelectric resonator arrays for tunable acoustic waveguides and metamaterials," J. Appl. Phys. **112**, 064902 (2012).
[37]X. Xu, M. V. Barnhart, X. Fang, J. Wen, Y. Chen, and G. Huang, "A nonlinear dissipative elastic metamaterial for broadband wave mitigation," Int. J. Mech. Sci. **164**, 105159 (2019).